NANO · MICRO small
www.small-journal.com

Synergetic Effect of Mo-Doped and Oxygen Vacancies Endows Vanadium Oxide with High-Rate and Long-Life for Aqueous Zinc Ion Battery

Daming Chen, Ming Yang, Yang Ming, Wei Cai, Shuo Shi, Yicai Pan, Xin Hu, Rujun Yu, Ziqi Wang, and Bin Fei**

Vanadium (V)-based oxides have garnered significant attention as cathode materials for aqueous zinc-ion batteries (AZIBs) due to their multiple valences and high theoretical capacity. However, their sluggish kinetics and low conductivity remain major obstacles to practical applications. In this study, Mo-doped V_2O_3 with oxygen vacancies (OVs, Mo-$V_2O_{3\text{-}x}$@NC) is prepared from a Mo-doped V-metal organic framework. Ex situ characterizations reveal that the cathode undergoes an irreversible phase transformation from Mo-$V_2O_{3\text{-}x}$ to Mo-$V_2O_{5\text{-}x}$·nH_2O and serves as an active material exhibiting excellent Zn^{2+} storage in subsequent charge-discharge cycles. Mo-doped helps to further improve cycling stability and increases with increasing content. More importantly, the synergistic effect of Mo-doped and OVs not only effectively reduces the Zn^{2+} migration energy barrier, but also enhances reaction kinetics, and electrochemical performance. Consequently, the cathode demonstrates ultrafast electrochemical kinetics, showing a superior rate performance (190.9 mAh g^{-1} at 20 A g^{-1}) and excellent long-term cycling stability (147.9 mAh g^{-1} at 20 A g^{-1} after 10000 cycles). Furthermore, the assembled pouch cell exhibits excellent cycling stability (313.6 mAh g^{-1} at 1 A g^{-1} after 1000 cycles), indicating promising application prospects. This work presents an effective strategy for designing and fabricating metal and OVs co-doped cathodes for high-performance AZIBs.

1. Introduction

Rechargeable aqueous zinc ion batteries (AZIBs) are gaining prominence in the realm of next-generation energy storage technologies due to their superior theoretical capacity (820 mAh g^{-1}), remarkable energy densities, inherent safety features, potential cost-effectiveness, and environmental sustainability.[1–5] However, the practical implementation of AZIBs is significantly impeded by the absence of appropriate cathode materials.[6–8] In addition, strong electrostatic attraction occurs between the embedded Zn^{2+} and the host lattice during the charge/discharge process, leading to hindered diffusion kinetics, low conductivity, and material structural collapse.[9] Consequently, the development of high-performance AZIBs fundamentally hinges on the design and synthesis of cathode materials with regulated structures and excellent electrochemical performance.

Up to now, substantial efforts have been dedicated to the development of cathode materials with high capacity and durability. These include vanadium (V)-based compounds,[7,10,11] manganese-based compounds,[12] Prussian blue analogs,[13] and organic materials.[14] V-based oxides (V_2O_5, V_2O_3, VO_2, and V_6O_{13}, *etc.*) have emerged as a focal point in AZIB cathode research, owing to their rich valence states, numerous crystal structures, and high theoretical capacity.[15,16] V_2O_5, in particular, is appealing due to its high theoretical capacity (589 mAh g^{-1}), but it typically undergoes severe structural degradation and slow Zn^{2+} intercalation/extraction kinetics, causing poor stability.[17,18] Recent studies have found that

---

D. Chen, Y. Ming, W. Cai, S. Shi, Y. Pan, X. Hu, R. Yu, B. Fei
Materials Synthesis and Processing Lab, School of Fashion and Textiles
The Hong Kong Polytechnic University
Kowloon, Hong Kong SAR 999077, P. R. China
E-mail: bin.fei@polyu.edu.hk

The ORCID identification number(s) for the author(s) of this article can be found under https://doi.org/10.1002/smll.202405168

DOI: 10.1002/smll.202405168

M. Yang
College of Chemistry and Environmental Engineering
Shenzhen University
Shenzhen 518060, P. R. China

Z. Wang
Department of Materials Science and Engineering, College of Chemistry and Materials Science
Jinan University
Guangzhou 511443, P. R. China
E-mail: wangzq@jnu.edu.cn

amorphous materials undergo smaller structural changes and offer more isotropic ion diffusion paths than crystalline structures, which is conducive to improving the Zn^{2+} diffusion kinetics and cyclic stability.[19] For instance, Wu et al. reported on an ultra-thin amorphous V_2O_5 electrode uniformly distributed on graphene, which exhibited short ion diffusion channels, excellent structural stability, and long-term cycling performance.[20] However, the electrical conductivity of the V-based oxides is subpar, resulting in unsatisfactory rate performance. To address the above shortcomings, various optimization strategies have been explored, including compounding with carbon materials, metal ion introduction, and oxygen defect engineering, *etc.*[8,14,21–23] Despite these efforts, electrodes prepared by mere physical contact with carbon materials fail to significantly enhance electron transfer efficiency.[24–26] With this in mind, the development of satisfactory cathode materials for AZIBs continues to pose a challenge.

Recently, researchers have made great achievements in the field of energy storage by using carbon-based composite materials derived from metal-organic frameworks (MOFs).[27–29] Various MOF-derived materials, such as V-MOF and Mn-MOF, have been extensively investigated as cathodes for AZIBs, resulting in a significant enhancement in rate performance. For example, Deng et al. developed a MOF-derived a-V_2O_5@C electrode with fast Zn^{2+} transport and high conductivity, where amorphous V_2O_5 is uniformly distributed in the carbon framework.[19] However, despite these achievements, the conductivity, kinetics, and rate performance of V-MOF-derived materials still fall short of the requirements for practical applications, necessitating further improvements. One approach to address this issue involves the incorporation of metal ions (such as Ni, Co, and Cu) or oxygen vacancies (OVs) into V-based oxides, which can modulate the electronic structure and subsequently enhance electrical conductivity.[8,24,30] Remarkably, materials such as $Mn_{0.04}V_2O_{5\text{-}x}\cdot 0.64\ H_2O$,[31] AlVO,[32] and $Mg_xV_2O_5\cdot nH_2O$[33] have demonstrated superior reaction kinetics and rate performance, which was attributed to the improvement of conductivity and the generation of OVs. It is reasonable to assume that the simultaneous introduction of metal ions and OVs into V-MOF-derived amorphous V_2O_5 will yield more unexpected results, which are rarely reported.

Herein, Mo-doped $V_2O_5\cdot nH_2O$@NC with OVs (Mo-$V_2O_{5\text{-}x}\cdot nH_2O$@NC) materials are synthesized via electrochemical activation of Mo-doped V-MOF-derived Mo-$V_2O_{3\text{-}x}$@NC. Upon charging to 1.6 V, the crystalline Mo-$V_2O_{3\text{-}x}$ transforms amorphous Mo-$V_2O_{5\text{-}x}\cdot nH_2O$ and serves as the active material for subsequent Zn^{2+} storage. The energy storage mechanism is thoroughly investigated using a suite of ex situ techniques, including XRD, XPS, EPR, SEM, and TEM. DFT calculations and experimental results indicate that the introduction of Mo ions and OVs not only reduces the reaction energy barrier, further promoting the reaction kinetics of Zn^{2+} storage but also improves the electrochemical performance. In addition, it is found that Mo-doped helps to further improve cycling stability. As expected, the optimal sample exhibits extraordinary rate performance and excellent long-term cycling stability. When assembled into a pouch cell, the sample also exhibits commendable electrochemical performance, showing its great application potential.

2. Results and Discussion

2.1. Theoretical Investigation

To comprehensively understand the impact of the coexistence of Mo-doped and OVs in Mo-$V_2O_{5\text{-}x}\cdot nH_2O$@NC on the electronic structure and Zn^{2+} storage performance, further analysis was conducted using density functional theory (DFT). As illustrated in Figure S1 (Supporting Information), three structural models of $V_2O_5\cdot nH_2O$, $V_2O_{5\text{-}x}\cdot nH_2O$ and Mo-$V_2O_{5\text{-}x}\cdot nH_2O$ are constructed. There are more electronic states on the Fermi level due to the coexistence of Mo-doped and OVs (**Figure** 1a–c), suggesting that Mo-$V_2O_{5\text{-}x}\cdot nH_2O$ has higher electronic conductivity than $V_2O_{5\text{-}x}\cdot nH_2O$ and $V_2O_5\cdot nH_2O$.[34,35] The enhanced conductivity of Mo-$V_2O_{5\text{-}x}\cdot nH_2O$ is further confirmed by the differential charge density, where cyan and yellow represent electron density accumulation and enrichment, respectively (Figure 1d–f). Compared with $V_2O_5\cdot nH_2O$ and $V_2O_{5\text{-}x}\cdot nH_2O$, the electron cloud of Mo-$V_2O_{5\text{-}x}\cdot nH_2O$ is larger, indicating more abundant electronic interactions and providing a greater charge concentration distribution for Zn^{2+} embedding.

Then, the adsorption energy (E_{ads}) of Zn^{2+} in $V_2O_5\cdot nH_2O$, $V_2O_{5\text{-}x}\cdot nH_2O$, and Mo-$V_2O_{5\text{-}x}\cdot nH_2O$ is calculated, as shown in Figure 1g (the inset represents the corresponding stable adsorption structure model). The E_{ads} value of Mo-$V_2O_{5\text{-}x}\cdot nH_2O$ (−31.8 eV) is more negative than that of $V_2O_{5\text{-}x}\cdot nH_2O$ (−27.3 eV) and $V_2O_5\cdot nH_2O$ (−22.4 eV), confirming that the synergistic effect of Mo-doped and OVs is beneficial to the adsorption of Zn^{2+}.[36] Furthermore, considering the calculated diffusion path and energy barrier (Figure 1h,i; Figure S2, Supporting Information), the energy barrier of Mo-$V_2O_{5\text{-}x}\cdot nH_2O$ is 0.23 eV, which is significantly lower than that of $V_2O_{5\text{-}x}\cdot nH_2O$ (0.36 eV) and $V_2O_5\cdot nH_2O$ (0.48 eV). This indicates that the coexistence of Mo-doped and OVs effectively reduces the diffusion energy barrier of Zn^{2+}, improving Zn^{2+} diffusion. Therefore, the introduction of Mo ions and OVs endows Mo-$V_2O_{5\text{-}x}\cdot nH_2O$ with a lower energy barrier and high electronic conductivity, which is beneficial to the kinetics of Zn^{2+} storage.

2.2. Structural Analysis

Figure 2 presents the synthesis schematic of Mo-doped V-MOF-3, Mo-$V_2O_{3\text{-}x}$@NC-3 and Mo-$V_2O_{5\text{-}x}\cdot nH_2O$@NC. Under similar experimental conditions, samples of V_2O_3@NC, $V_2O_{3\text{-}x}$@NC, Mo-$V_2O_{3\text{-}x}$@NC-1, Mo-$V_2O_{3\text{-}x}$@NC-2, and Mo-$V_2O_{3\text{-}x}$@NC-4 can be synthesized by incorporating varying amounts of phosphomolybdic acid (PMA, see the experimental section for details). Then, when Mo-$V_2O_{3\text{-}x}$@NC-3 is charged to 1.6 V, Mo-$V_2O_{5\text{-}x}\cdot nH_2O$@NC is produced via electrochemical activation. Succinctly, precursors of V-MOF and Mo-doped V-MOF-*n* (*n* = 1, 2, 3, and 4) can be synthesized through a straightforward hydrothermal method using 1,4-Naphthalenedicarboxylic acid (1,4-NDC), Vanadium (III) chloride, and a certain amount of PMA (**Figure** 3a,b; Figure S3, Supporting Information). All the aforementioned materials exhibit a nanorod structure. Intriguingly, the particle size of Mo-doped V-MOF-*n* is significantly smaller than that of V-MOF, indicating that the introduction of the Mo ions can alter the size of V-MOF.

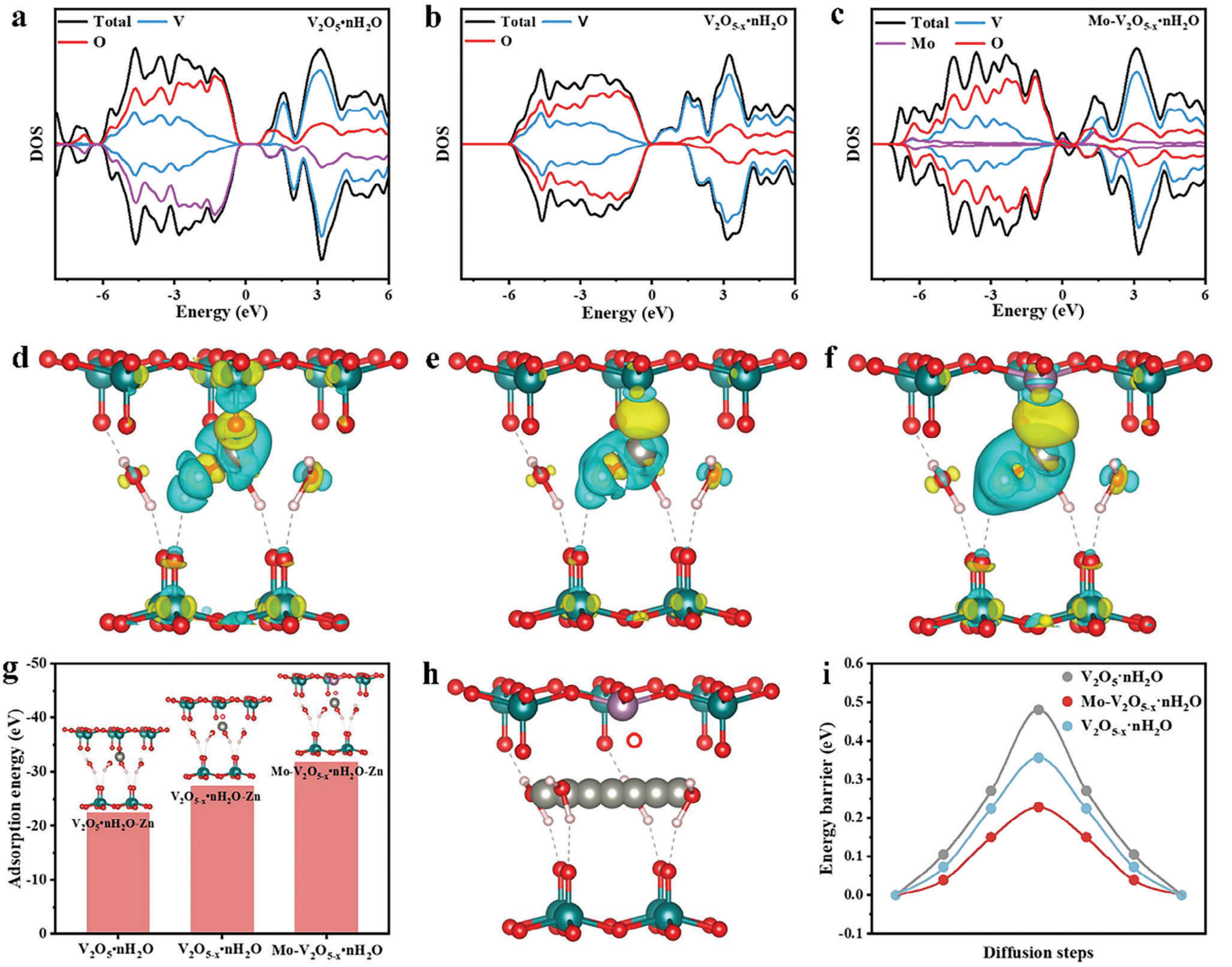

Figure 1. The DFT calculation results. The density of states (DOS) of a) $V_2O_5 \cdot nH_2O$, b) $V_2O_{5\text{-}x} \cdot nH_2O$, and c) Mo-$V_2O_{5\text{-}x} \cdot nH_2O$. Differential charge density with Zn^{2+} intercalation in d) $V_2O_5 \cdot nH_2O$ e) $V_2O_{5\text{-}x} \cdot nH_2O$, and f) Mo-$V_2O_{5\text{-}x} \cdot nH_2O$. g) The adsorption energy of Zn^{2+} in $V_2O_5 \cdot nH_2O$, $V_2O_{5\text{-}x} \cdot nH_2O$, and Mo-$V_2O_{5\text{-}x} \cdot nH_2O$. h) Possible migration pathways for Zn^{2+} in Mo-$V_2O_{5\text{-}x} \cdot nH_2O$. i) Calculated Zn^{2+} diffusion barriers in $V_2O_5 \cdot nH_2O$, $V_2O_{5\text{-}x} \cdot nH_2O$, and Mo-$V_2O_{5\text{-}x} \cdot nH_2O$.

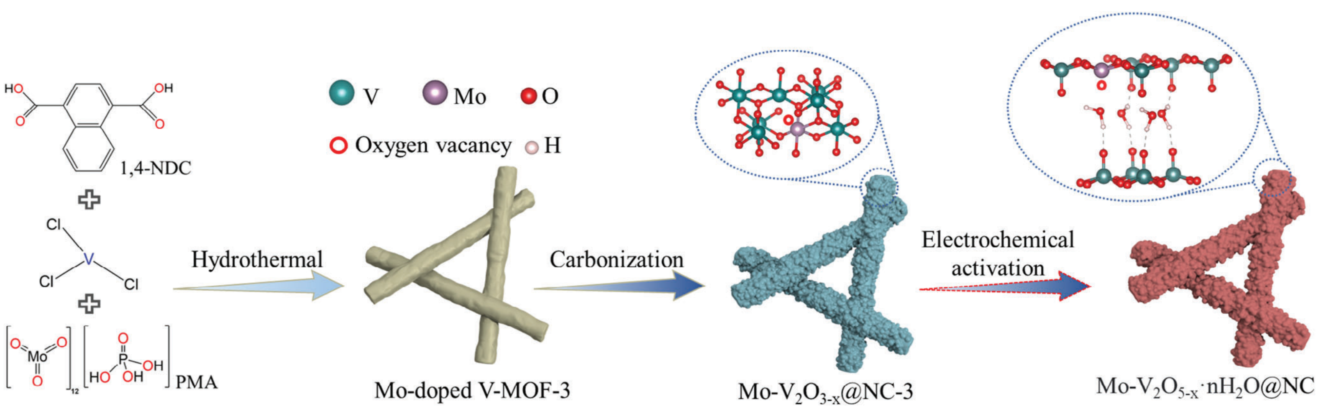

Figure 2. Schematic illustration for the synthesis of nanocomposites.

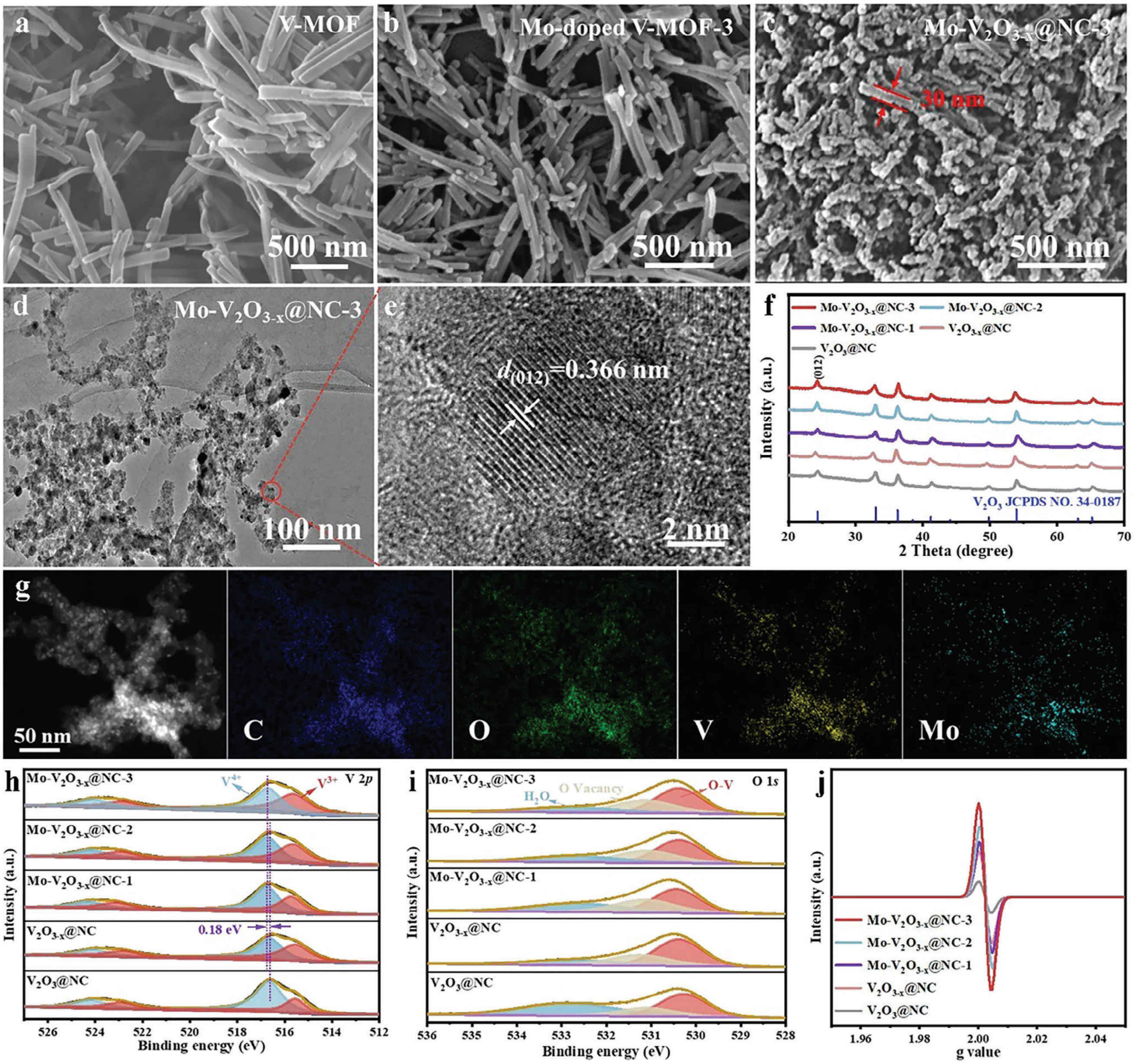

Figure 3. Morphological and structural characterization of nanocomposites. a–c) SEM images of V-MOF, Mo-doped V-MOF-3, and Mo-V$_2$O$_{3-x}$@NC-3, respectively. d,e) TEM and HRTEM images of Mo-V$_2$O$_{3-x}$@NC-3. f) XRD pattern of V$_2$O$_3$@NC, V$_2$O$_{3-x}$@NC, V$_2$O$_{3-x}$@NC, Mo-V$_2$O$_{3-x}$@NC-1, Mo-V$_2$O$_{3-x}$@NC-2 and Mo-V$_2$O$_{3-x}$@NC-3, respectively. g) HAADF-STEM image of Mo-V$_2$O$_{3-x}$@NC-3 and the elemental distribution of C, O, V, and Mo. h,i) High-resolution XPS spectra of V 2*p* and O 1s. j) EPR spectra of V$_2$O$_3$@NC, V$_2$O$_{3-x}$@NC, Mo-V$_2$O$_{3-x}$@NC-1, Mo-V$_2$O$_{3-x}$@NC-2, and Mo-V$_2$O$_{3-x}$@NC-3, respectively.

Then, V$_2$O$_3$@NC, V$_2$O$_{3-x}$@NC, Mo-V$_2$O$_{3-x}$@NC-1, Mo-V$_2$O$_{3-x}$@NC-2, Mo-V$_2$O$_{3-x}$@NC-3 and Mo-V$_2$O$_{3-x}$@NC-4 are obtained by calcination at 800 °C for 6 h in Ar/H$_2$ or Ar gas, respectively. Scanning Electron Microscope (SEM) morphologies confirm that post-high-temperature calcination, the obtained samples form nanorods with a minor diameter (≈30 nm), which can shorten the transfer distance of Zn^{2+} and speed up the reaction kinetics (Figure 3c; Figure S4, Supporting Information). Transmission Electron Microscopy (TEM) images (Figure 3d; Figure S5, Supporting Information) further confirm that the introduction of Mo ions can reduce the size of the sample. Subsequent HRTEM image (Figure 3e) observation shows that the lattice fringe spacing is ≈0.366 nm, which can be attributed to the (012) plane of the V$_2$O$_3$ phase.[37]

To determine the crystal structure of the prepared samples, X-ray diffraction (XRD) tests were performed. The XRD spectra (Figure 3f) reveal a perfect alignment of all diffraction peaks in V$_2$O$_3$@NC and V$_2$O$_{3-x}$@NC with the V$_2$O$_3$ phase (JCPDF No. 34–0187). After the introduction of the Mo ions, Mo-V$_2$O$_{3-x}$@NC-1, Mo-V$_2$O$_{3-x}$@NC-2, and Mo-V$_2$O$_{3-x}$@NC-3 still maintain the V_2O_3 phase, suggesting the absence of any additional hybrid formations. Meanwhile, the interlayer distance of V_2O_3 is ≈0.366 nm according to the characteristic (012) diffraction peak, which is consistent with the HRTEM result. However, an increase in PMA content leads to the formation of MoO_3 impurities in the material (Figure S6, Supporting Information), possibly attributable to the alteration of the original material's crystal structure by the introduction of a substantial quantity of Mo ions. Therefore, the following discussion mainly focuses on V_2O_3@NC, $V_2O_{3\text{-}x}$@NC, Mo-$V_2O_{3\text{-}x}$@NC-1, Mo-$V_2O_{3\text{-}x}$@NC-2, and Mo-$V_2O_{3\text{-}x}$@NC-3. Moreover, the high-angle annular dark-field scanning TEM (HAADF-STEM) image in Figure 3g confirms the uniform distribution of C, O, V, and Mo elements in Mo-$V_2O_{3\text{-}x}$@NC-3, indicating the successful introduction of Mo ions. The N_2 adsorption/desorption isotherm (Figure S7, Supporting Information) demonstrates that the synthesized samples possess mesoporous structures. All samples exhibit large specific surface areas, which are conducive to enhancing interface reactions, ion diffusion channels, and active sites.[38] Raman spectra (Figure S8, Supporting Information) show that the prepared samples have typical characteristic peaks of V_2O_3, which are located at 142, 283, 405, 689, and 989 cm^{-1}, respectively, once again proving the successful preparation of V_2O_3 composite materials.[39]

X-ray photoelectron spectroscopy (XPS) measurements were employed to further investigate the surface element composition and chemical state of the synthesized samples. The XPS spectra (Figure S9, Supporting Information) show that the signal peaks of C, N, O, and V can be detected in all samples. In addition, Mo peaks are detected in Mo-$V_2O_{3\text{-}x}$@NC-1, Mo-$V_2O_{3\text{-}x}$@NC-2, and Mo-$V_2O_{3\text{-}x}$@NC-3 samples, again confirming the successful introduction of Mo ions. The high-resolution V 2*p* spectra of V_2O_3@NC and $V_2O_{3\text{-}x}$@NC (Figure 3h) exhibit the two peaks at 515.8 and 522.8 eV, corresponding to V^{3+}, while the peaks at 516.7 and 524.2 eV are attributed to V^{4+}.[40,41] Following the introduction of the Mo ions, a noticeable shift to higher binding energy is observed for V^{4+}, suggesting an electronic interaction between V_2O_3 and Mo and a consequent alteration in the electronic structure of V.[42,43] The O1*s* spectrum (Figure 3i) can be decomposed into three peaks at 530.4, 531.3, and 532.8 eV, representing lattice oxygen (O—V bond), OVs, and oxygen in absorbed water, respectively.[17,44,45] Compared with V_2O_3@NC, the peak area ratio of OVs in $V_2O_{3\text{-}x}$@NC is larger, indicating that Ar/H_2 gas treatment helps to increase the OVs concentration. Concurrently, the peak area ratio of OVs in Mo-doped samples (Mo-$V_2O_{3\text{-}x}$@NC-1, Mo-$V_2O_{3\text{-}x}$@NC-2, and Mo-$V_2O_{3\text{-}x}$@NC-3) increases, indicating that Mo-doped can also effectively increase the concentration of OVs, which effectively improve the reaction kinetics. As evidenced by Table S1 (Supporting Information), a slight rise in the concentration of OVs accompanies an increase in Mo-doped content. Furthermore, the OVs of the samples were also studied through electron paramagnetic resonance (EPR) measurements (Figure 3j). The results also show that Mo-$V_2O_{3\text{-}x}$@NC-3 has the highest OVs concentration, indicating that the OVs concentration can be further increased with the increase of Mo-doped content, which well confirms the above O1*s* spectrum results. The Mo 3*d* spectra of Mo-$V_2O_{3\text{-}x}$@NC-1, Mo-$V_2O_{3\text{-}x}$@NC-2, and Mo-$V_2O_{3\text{-}x}$@NC-3 samples (Figure S10, Supporting Information) display two peaks at 232.8 eV (Mo^{6+} $3d_{5/2}$) and 235.9 eV (Mo^{6+} $3d_{3/2}$), evidencing the introduction of Mo ions.[46] Additionally, according to the XPS and inductively coupled plasma (ICP, Table S2, Supporting Information) results, the Mo content in Mo-$V_2O_{3\text{-}x}$@NC-1, Mo-$V_2O_{3\text{-}x}$@NC-2, and Mo-$V_2O_{3\text{-}x}$@NC-3 samples is ≈5%, ≈7.5%, and ≈10%, respectively, which is close to the ratio of added raw materials.

2.3. Electrochemical Performance

The electrochemical performance of all samples was evaluated using CR2023-type coin cells. The rate performance of V_2O_3@NC, $V_2O_{3\text{-}x}$@NC, Mo-$V_2O_{3\text{-}x}$@NC-1, Mo-$V_2O_{3\text{-}x}$@NC-2, and Mo-$V_2O_{3\text{-}x}$@NC-3 electrodes at varying current densities is depicted in **Figure 4**a. Obviously, Mo-$V_2O_{3\text{-}x}$@NC-3 exhibits superior rate performance, which delivers specific capacities of 424.3, 413.2, 399.3, 389.5, 376.3, 340.4, 296.1, and 261.5 mAh g^{-1} at current densities ranging from 0.1 to 10 A g^{-1}, respectively. Even at the ultra-high current density of 20 A g^{-1}, it retains a specific capacity of 190.9 mAh g^{-1}. Upon reverting the current density to 0.1 A g^{-1}, the specific capacity remains at 423.5 mAh g^{-1}, demonstrating excellent reversibility and structural stability. Compared with the introduction of OVs alone or without OVs, the coexistence of Mo-doped and OVs is more beneficial in improving the rate performance and specific capacity. Furthermore, the Mo-$V_2O_{3\text{-}x}$@NC-3 electrode also exhibits remarkable rate performance in comparison to other previously documented V-based cathode materials, as shown in Figure 4b.[9,34,37,41,47–52] Impressively, the Mo-$V_2O_{3\text{-}x}$@NC-3 electrode exhibits high energy and power density, as shown in the Ragone plot (Figure S11, Supporting Information). It provides a significant energy density of 267 Wh kg^{-1} at a power density of 21.4 kW kg^{-1}, which is superior to most of the recently reported AZIBs.

The superior rate performance of the Mo-$V_2O_{3\text{-}x}$@NC-3 electrode significantly depends on its kinetics, thereby stimulating research on its capacitive characteristics. Figure S12 (Supporting Information) shows the CV curves of V_2O_3@NC, $V_2O_{3\text{-}x}$@NC, Mo-$V_2O_{3\text{-}x}$@NC-1, Mo-$V_2O_{3\text{-}x}$@NC-2, and Mo-$V_2O_{3\text{-}x}$@NC-3 electrodes within a scanning range of 0.2–1.0 mV s^{-1}. To analyze faradic contribution and pseudo-capacitance behavior in electrode materials, the electrochemical storage process of CV data at different scan rates is used to analyze through the power-law equation ($i = av^b$).[53] Here, a and b are adjustable parameters, and v represents the scan rate. As depicted in Figure S13 (Supporting Information), all b values fall within the range of 0.5-1, indicating that the electrochemical reaction in Mo-$V_2O_{3\text{-}x}$@NC-3 electrode is dually controlled by capacitance control and diffusion control. Then, the contribution ratio of the pseudo-capacitance is analyzed by the following formula: $i\,(V) = k_1\,v + k_2 v^{1/2}$, where $k_1 v$ and $k_2 v^{1/2}$ denote the contribution of the pseudo-capacitance and diffusion process, k_1 and k_2 are constants at a certain potential.[6] Figure 4c and Figure S14 (Supporting Information) display that the pseudo-capacitance contribution ratio of Mo-$V_2O_{3\text{-}x}$@NC-3 electrode (85.3%) surpasses those of the V_2O_3@NC (65.9%), $V_2O_{3\text{-}x}$@NC (68.6%), Mo-$V_2O_{3\text{-}x}$@NC-1 (70.3%) and Mo-$V_2O_{3\text{-}x}$@NC-2 (76.8%) electrodes at 1.0 mV s^{-1}, indicating its superior electrochemical kinetics, which corroborates the high-rate performance observed in Figure 4a. Moreover, as the scan rate increases (Figure S15, Supporting Information), the contribution of the capacitance contribution ratio

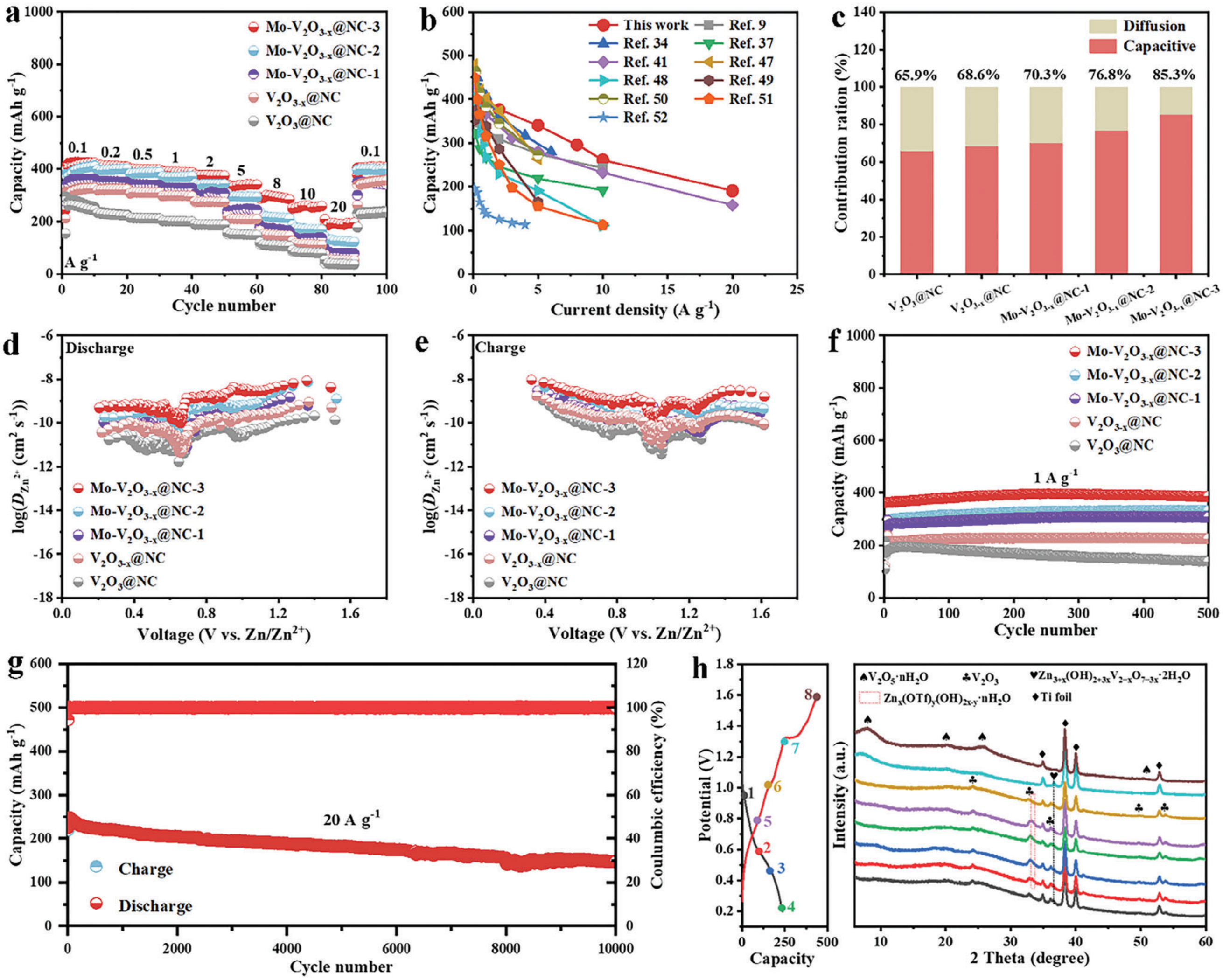

Figure 4. Electrochemical performances of the cathodes. a) Rate performances of V$_2$O$_3$@NC, V$_2$O$_{3-x}$@NC, Mo-V$_2$O$_{3-x}$@NC-1, Mo-V$_2$O$_{3-x}$@NC-2, and Mo-V$_2$O$_{3-x}$@NC-3. b) Rate performance of Mo-V$_2$O$_{3-x}$@NC-3 in comparison with literature. c) Ratio of capacitive contribution of V$_2$O$_3$@NC, V$_2$O$_{3-x}$@NC, Mo-V$_2$O$_{3-x}$@NC-1, Mo-V$_2$O$_{3-x}$@NC-2, and Mo-V$_2$O$_{3-x}$@NC-3 at 1.0 mV s^{-1}. d,e) Zn^{2+} diffusion coefficients versus different discharge/charge states; f) Cycling performances of V$_2$O$_3$@NC, V$_2$O$_{3-x}$@NC, Mo-V$_2$O$_{3-x}$@NC-1, Mo-V$_2$O$_{3-x}$@NC-2, and Mo-V$_2$O$_{3-x}$@NC-3 at 1 A g^{-1}. g) Long-cycling performance of Mo-V$_2$O$_{3-x}$@NC-3 at 20 A g^{-1}. h) Ex situ XRD patterns of Mo-V$_2$O$_{3-x}$@NC-3 at different voltage states during the initial charge/discharge processes at 0.2 A g^{-1}.

progressively increases, signifying the dominance of capacitance control in the electrochemical reaction. The high capacitance of Mo-V$_2$O$_{3-x}$@NC-3 is mainly due to the synergistic effect of Mo-doped and OVs, which effectively increases the conductivity and enhances the charge storage capability of the reversible pseudo-capacitance.

The galvanostatic intermittent titration technique (GITT) was employed to further examine the diffusion coefficients of Zn^{2+} ($D_{Zn^{2+}}$), as per Equation S1 (Supporting Information), as shown in Figure S16 (Supporting Information).[54] The GITT data in Figure 4d,e and Figure S16 (Supporting Information) confirm that the Zn^{2+} diffusion coefficient of the Mo-V$_2$O$_{3-x}$@NC-3 electrode (during the entire intercalation process varies from 10.18 × 10^{-9} to 8.19 × 10^{-8} cm^2 s^{-1}) is significantly higher than that of the V$_2$O$_3$@NC, V$_2$O$_{3-x}$@NC, V$_2$O$_{3-x}$@NC, Mo-V$_2$O$_{3-x}$@NC-1, and Mo-V$_2$O$_{3-x}$@NC-2 electrodes. This result shows that the Mo-V$_2$O$_{3-x}$@NC-3 has a faster Zn^{2+} diffusion efficiency and reaction kinetics. Except for the GITT test, EIS tests were also conducted on the samples, as illustrated in Figure S17 (Supporting Information). The charge-transfer resistance (Rct) of the Mo-V$_2$O$_{3-x}$@NC-3 electrode is found to be lower than those of the V$_2$O$_3$@NC, V$_2$O$_{3-x}$@NC, Mo-V$_2$O$_{3-x}$@NC-1, and Mo-V$_2$O$_{3-x}$@NC-2 electrodes, illustrating a higher electrical conductivity. Obviously, the coexistence of Mo-doped and OVs effectively improves the conductivity and electrochemical reaction kinetics.

Figure S18 (Supporting Information) shows the cyclic test of the electrodes at a low current density of 0.2 A g^{-1}. The discharge capacity and Coulumbic efficiencies (CEs) gradually enhance during the cycle, indicating the activation process of the electrode material. More significantly, the long-cycle performance of the electrodes is also evaluated, as shown in Figure 4f. Evidently, the Mo-V$_2$O$_{3-x}$@NC-3 electrode shows the highest specific capacity

(386.8 mAh g^{-1}) after 500 cycles at a current density of 1 A g^{-1}. Even at a high current density of 20 A g^{-1} (Figure 4g; Figure S19, Supporting Information), the specific capacity output after 10 000 cycles is 147.9 mAh g^{-1}, with a capacity retention rate of 70.1%, which is higher than V_2O_3@NC (41.2%), V_2O_{3-x}@NC (43.8%), Mo-V_2O_{3-x}@NC-1 (60.5%) and Mo-V_2O_{3-x}@NC-2 (62.7%). This result indicates that the introduction of Mo ions is beneficial to increase the cycling stability, and it increases with the increase of the content. Nevertheless, although the introduction of OVs improves the specific capacity and rate performance to a degree, the cycling stability is not satisfactory. Therefore, the Mo-V_2O_{3-x}@NC-3 electrode possesses excellent rate performance and cycling stability due to the synergistic effect of Mo-doped and OVs, which is more effective than the sole introduction of OVs. In addition, the Mo-V_2O_{3-x}@NC-3 electrode still maintains the nanorod structure after 100 cycles at a current density of 1 A g^{-1}, fully proving its excellent structural stability (Figure S20, Supporting Information). When compared to other V-based oxide cathode materials documented in recent literature, Mo-V_2O_{3-x}@NC-3 continues to display exceptional electrochemical performance, thereby emerging as a promising electrode material (Table S3, Supporting Information).

The electrochemical behavior of Mo-V_2O_{3-x}@NC-3 as a cathode material is evaluated through CV curves. In the initial cycle of the CV curve for the Mo-V_2O_{3-x}@NC-3 electrode (Figure S21, Supporting Information), two prominent oxidation peaks at 1.29 and 1.45 V appear in the reverse scan but are absent in the following cycles, indicating that electrochemical oxidation has occurred and led to irreversible phase transformation. To elucidate the cause of this phase transformation, ex situ XRD analysis is performed (Figure 4h). During the initial discharge process, the electrode material maintains the crystal structure of V_2O_3. However, a significant phase change occurs between 1.3–1.6 V during charging. In the fully charged state, the diffraction peaks at 8.1°, 20.3°, 25.7°, and 50.7° match well with $V_2O_5{\cdot}nH_2O$.[19,47,55] Therefore, when charged to 1.6 V, V_2O_{3-x} undergoes electrochemical activation to transform into $V_2O_5{\cdot}nH_2O$ with OVs ($V_2O_{5-x}{\cdot}nH_2O$). At the same time, other types of diffraction peaks were observed in the ex situ XRD of the first cycle, which will be discussed later. In addition, two pairs of redox peaks appear in the next two cycles, corresponding to the valence state changes of V from V^{5+} to V^{4+} and V^{4+} to V^{3+}, demonstrating a multi-step conversion reaction mechanism caused by the Zn^{2+} intercalation/deintercalation.[19,37] A similar phase transformation is also distinctly reflected in the initial five-period charge and discharge curves at a current of 0.2 A g^{-1}, as shown in Figure S22 (Supporting Information). Apart from the first cycle, the remaining curves basically overlap, indicating that the subsequent oxidation product has efficient and stable Zn^{2+} storage performance. Afterward, to understand the morphology structure, and composition of the oxidation product after the first cycle, SEM and TEM characterizations were performed. It can be seen from the SEM image (Figure S23, Supporting Information) and TEM image (Figure S24a, Supporting Information) that the electrode material still maintains the nanorod structure after the first cycle. The HRTEM image (Figure S24b, Supporting Information) shows an amorphous structure. Furthermore, C, O, V, and Mo elements are uniformly distributed on the surface of the above product, as shown in Figure S24c (Supporting Information). Therefore, the obtained electrochemically activated product is identified as Mo-$V_2O_{5-x}{\cdot}nH_2O$@NC with a nanorod structure. Overall, the synergistic effect of Mo-doped and OVs in the Mo-$V_2O_{5-x}{\cdot}nH_2O$@NC electrode not only effectively improves the kinetics and conductivity, but also endows outstanding rate performance and long-cycling stability, which is consistent with the theoretical findings.

To deeply understand the Zn^{2+} storage mechanism of the Mo-$V_2O_{5-x}{\cdot}nH_2O$@NC derived from Mo-V_2O_{3-x}@NC-3, ex situ XRD tests were performed during the second cycle (**Figure 5a**). As mentioned above (Figure 4h), Mo-V_2O_{3-x}@NC-3 undergoes a transformation into Mo-$V_2O_{5-x}{\cdot}nH_2O$@NC after the first charge. During the discharge process, the peak intensity of $V_2O_5{\cdot}nH_2O$ becomes weaker, and two new peaks appear at ≈33.1° and 36.6°, corresponding to the diffraction peak of $Zn_x(OTf)_y(OH)_{2x-y}{\cdot}nH_2O$ and $Zn_{3+x}(OH)_{2+3x}V_{2-x}O_{7-3x}{\cdot}2H_2O$, respectively, which is consistent with the previous literature.[47,56,57] The formation of $Zn_x(OTf)_y(OH)_{2x-y}{\cdot}nH_2O$ and $Zn_{3+x}(OH)_{2+3x}V_{2-x}O_{7-3x}{\cdot}2H_2O$ is primarily attributed to the by-products of the reaction involving OH^-, $Zn(CF_3SO_3)_2$ and Zn^{2+} with $V_2O_5{\cdot}nH_2O$.[58,59] Concurrently, the peak position of $V_2O_5{\cdot}nH_2O$ slightly shifts to the left, which may be caused by the lattice distortion induced by the co-insertion of protons (H^+) and Zn^{2+}.[60] Upon discharging to 0.2 V, the diffraction peak located at ≈8° disappears, possibly due to the low crystallinity of nano-scale $Zn_xV_2O_5{\cdot}nH_2O$.[55] In the process of charging to 1.6 V, the $Zn_x(OTf)_y(OH)_{2x-y}{\cdot}nH_2O$ and $Zn_{3+x}(OH)_{2+3x}V_{2-x}O_{7-3x}{\cdot}2H_2O$ diffraction peaks disappear, and the peak positions of $V_2O_5{\cdot}nH_2O$ are recovered, thus proving its good reversibility. Additionally, Figure S23 (Supporting Information) shows the XRD patterns of the above electrode materials after different cycles at a current density of 1 A g^{-1}. The diffraction peak is basically consistent with the corresponding product when charged to 1.6 V (Figure 5a), indicating its superior cycling stability and reversibility.

Ex situ XPS was used to analyze the changes in elemental composition and valence state of the Mo-$V_2O_{5-x}{\cdot}nH_2O$@NC electrode. As shown in Zn 2*p* spectra (Figure 5b), the pristine electrode does not exhibit any Zn signal. When re-discharged to 0.2 V following two cycles, two strong peaks located at 1045.6 eV (Zn $2p_{3/2}$) and 1021.8 eV (Zn $2p_{1/2}$) are detected, further proving the insertion of Zn^{2+}. Then, when charged to 1.6 V, the intensity of the Zn signal peak decreases significantly, which is attributed to the deintercalation of Zn^{2+}. In the V *2p* spectrum (Figure 5c), the pristine electrode exhibits two peaks, belonging to V^{3+} and V^{4+}. Upon discharge to 0.2 V, three peaks located at 516.0, 516.8, and 517.6 eV corresponded to the V^{3+}, V^{4+}, and V^{5+}, respectively. In the fully charged state, there are only two valence peaks of V^{5+} and V^{4+}, the peak of V^{3+} completely disappears, indicating that low valence V is reversibly oxidized.[61] As for the O 1*s* spectrum (Figure 5d), three peaks located at 530.4, 531.6, and 532.9 eV belong to the O—V bond, OVs, and H_2O, respectively. Compared with other states, the intensity of the H_2O peak increases when discharged to 0.2 V, mainly due to the intercalation of H^+ in V_2O_5 and forms bound water with oxygen.[47,62] Moreover, the binding energy of OVs slightly shifts toward the high binding energy, probably due to the OVs inducing many lone pairs of electrons and changing the arrangement of electrons.[44] Interestingly, when charged to 1.6 V, the H_2O peak still exists, indicating that the H_2O molecules will not be completely separated during the activation process, which is beneficial to the

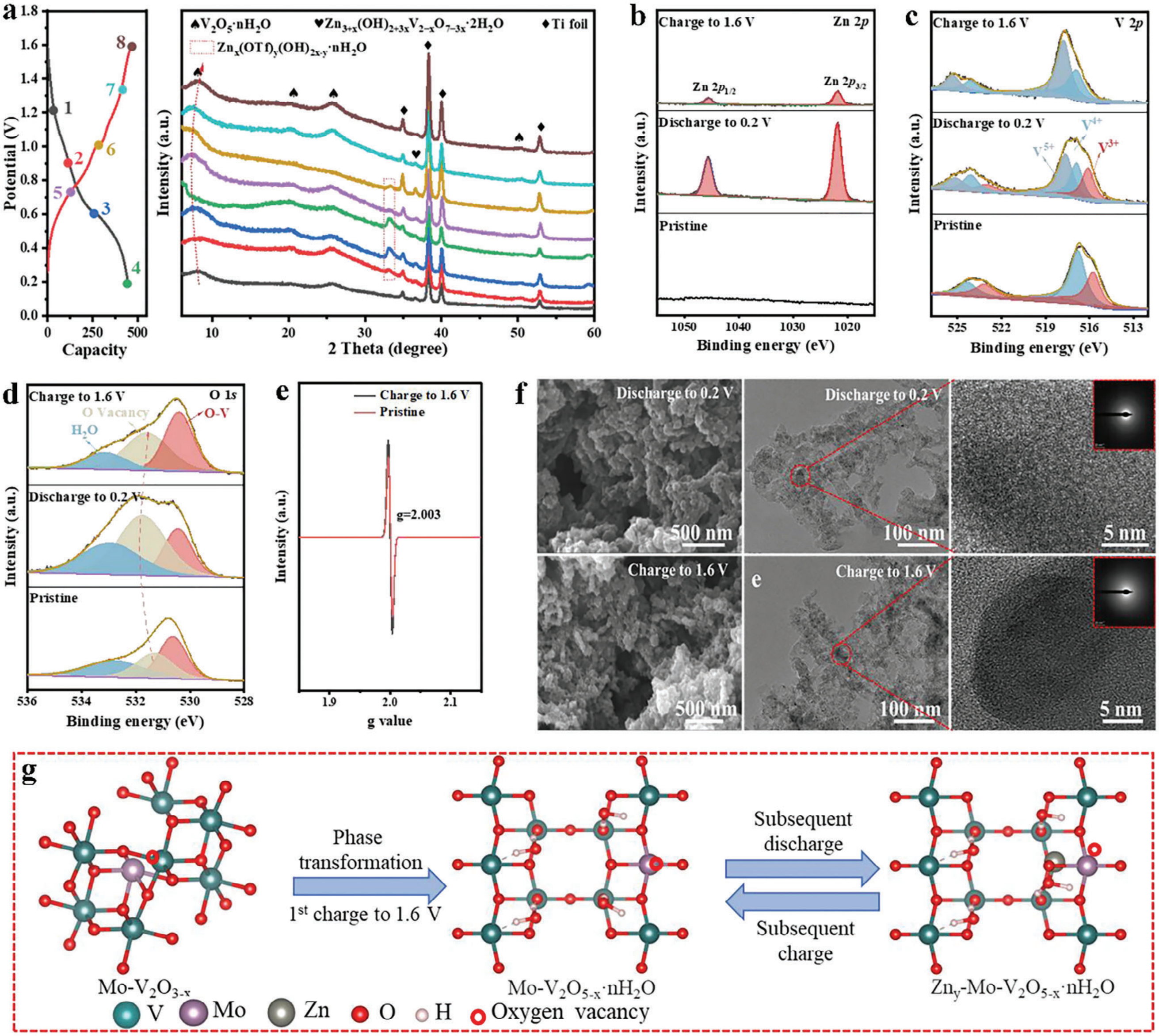

Figure 5. The charge storage mechanism of Mo-V$_2$O$_{3-x}$@NC-3 after the second cycle. a) Ex situ XRD patterns of Mo-V$_2$O$_{5-x}$·nH$_2$O@NC at different voltage states during the second cycle of charge/discharge processes at 0.2 A g^{-1}. b–d) The corresponding ex situ XPS spectra of Zn 2*p* (b), V 2*p* (c) and O 1*s* (d). e) Ex situ EPR spectra. f) SEM, TEM, HRTEM, and corresponding selected area diffraction (SAED) pattern of Mo-V$_2$O$_{5-x}$·nH$_2$O at different states. g) Schematic illustration of the reaction mechanism.

stability of the Zn^{2+} diffusion process. In addition, the OVs concentration is higher relative to the pristine electrode. Based on these observations, EPR measurements were performed on these two samples (Figure 5e). The cycled electrode also exhibits a higher signal. Therefore, the O 1*s* and EPR results reveal that Mo-V$_2$O$_{5-x}$·nH$_2$O@NC maintains high stability of OVs after cycling, which will effectively increase active sites and improve diffusion kinetics of Zn^{2+}.[54] Figure 5f shows the SEM, TEM, HRTEM, and corresponding SAED images of discharge to 0.2 V and charge to 1.6 V following the second cycle, respectively. All samples exhibit nanorod structures, indicating good structural stability. Subsequently, no lattice fringes are detected from the HRTEM and SAED images, further indicating that the formed Mo-V$_2$O$_{5-x}$·nH$_2$O@NC possesses an amorphous structure. Accordingly, the energy storage mechanism of the cathode material is shown in Figure 5g. Mo-V$_2$O$_{3-x}$ undergoes phase transformation to form amorphous Mo-V$_2$O$_{5-x}$·nH$_2$O when initially charged to 1.6 V, and the intercalation/extraction of Zn^{2+} is highly reversible at the subsequent charge/discharge process.

2.4. Electrochemical Performance of Full-Cell Pouch Cell

Given the superior electrochemical performance of the Mo-V$_2$O$_{3-x}$@NC-3 derived Mo-V$_2$O$_{5-x}$·nH$_2$O@NC electrode, an AZBs pouch cell was assembled to demonstrate its practical

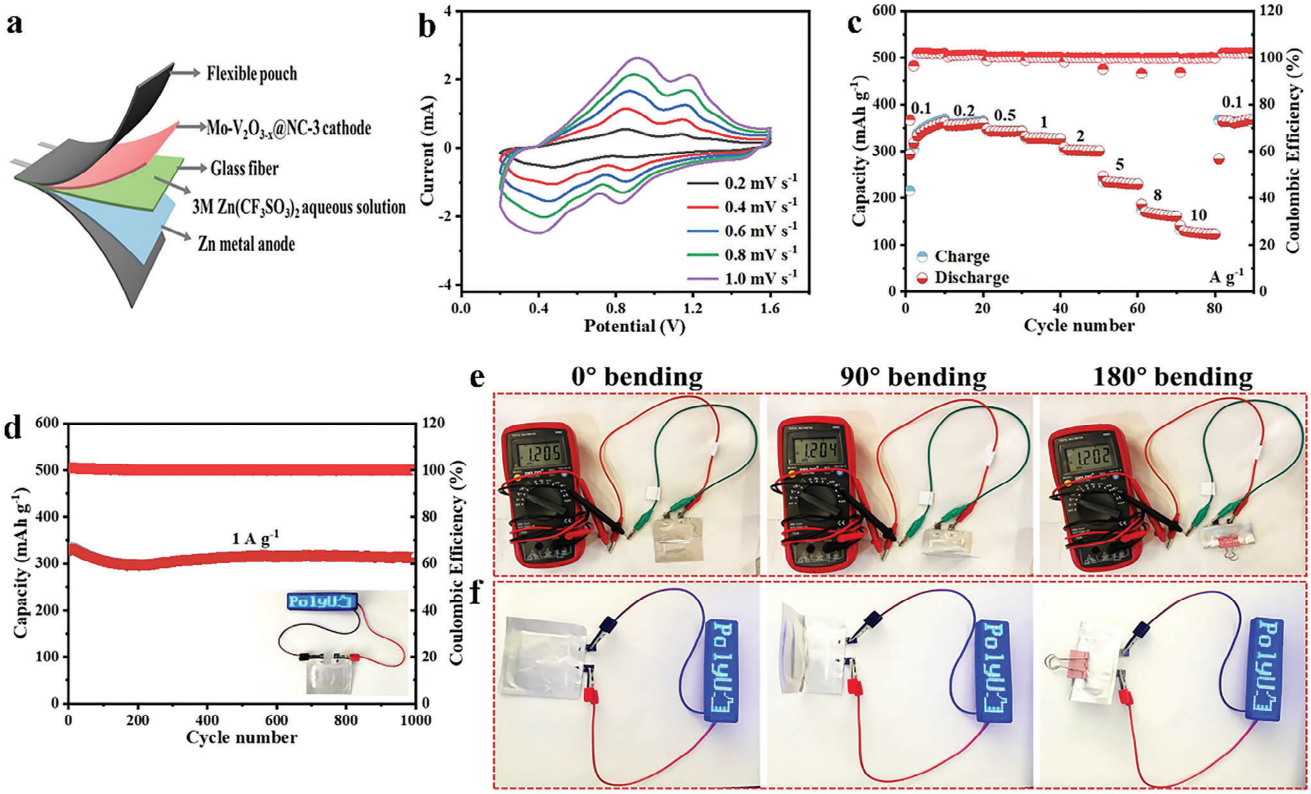

Figure 6. Electrochemical performance of pouch cell. a) Schematic diagram of AZBs pouch cell. b) CV curves of AZBs pouch cells at various scan rates. c) Rate performances of AZBs pouch cell; d) Cycling performance of AZBs pouch cell at a current density of 1 A g^{-1}. e) Open circuit voltage and f) The working condition of the pouch cell under the 0°, 90°, and 180° bending states.

application (**Figure 6a**). The electrochemical kinetics of AZIBs pouch cells are examined by testing the CV curves at various scan rates, as depicted in Figure 6b. The capacitance contribution reaches 83.1% at 1.0 mV s^{-1} (Figure S26a, Supporting Information). The capacitance contribution (Figure S26b, Supporting Information) increases with the increase of the scanning rate, indicating that capacitance control is dominant, which is conducive to improving electrochemical kinetics and rate performance. Figure 6c reveals that the capacities of AZIBs pouch cells range from 360.2 to 126.1 mAh g^{-1} as the current density augments from 0.1 to 10 A g^{-1}. As the current density returns to 0.1 A g^{-1}, the specific capacity recovers to 362.4 mAh g^{-1}, indicating that the AZIBs pouch cell has excellent rate performance and good reversibility. In addition, the cycling stability of AZIBs pouch cells is also evaluated (Figure 6d). Following 1000 cycles at a current density of 1 A g^{-1}, the specific capacity remains at 313.6 mAh g^{-1} with nearly 100% coulombic efficiency, implying excellent structural stability. It is worth mentioning that the open circuit voltage of the AZIBs pouch cell can be maintained at ≈1.2 V under different bending levels, indicating good flexibility. (Figure 6e). Moreover, when the AZIBs pouch cell is charged to 1.6 V, it can also power the LED under different bending conditions (Figure 6f). Consequently, the electrode shows promising application prospects in energy storage devices.

3. Conclusion

In summary, we have successfully synthesized the Mo-$V_2O_{5-x}\cdot nH_2O$@NC electrode material by inducing the phase transformation of Mo-V_2O_{3-x}@NC-3 through electrochemical activation. According to DFT calculations and experimental results, the synergistic effect of Mo-doped and OVs improves the rate performance and capacity, reduces the energy barrier, and facilitates reaction kinetics. In addition, Mo-doped is conducive to improving the stability of electrode materials and increases with the increase of content. Moreover, ex situ analysis results demonstrate that the intercalation/extraction of Zn^{2+} in the Mo-$V_2O_{5-x}\cdot nH_2O$@NC electrode is highly reversible, and further analyzes its energy storage mechanism. As a result, the optimal cathode delivers high-rate performance (424.3 mAh g^{-1} at 0.1 A g^{-1} and 190.9 mAh g^{-1} at 20 A g^{-1}, respectively), and good long-term cycling stability (147.9 mAh g^{-1} at 20 A g^{-1} after 10 000 cycles, and the capacity retention rate is 70.1%), outperforming other reported V-based cathode materials. Furthermore, the as-prepared pouch cell also demonstrates exceptional electrochemical performance and potential applications. More importantly, this work can provide new avenues for the development of high-performance composite cathode materials.

Supporting Information

Supporting Information is available from the Wiley Online Library or from the author.

Acknowledgements

The authors would like to thank the financial support from the PolyU Postdoc Matching Fund 1-W34P, ITF project ITP/023/22TP, PolyU RCRE fund 1-BBCB, and IWEAR fund 1-CD8E.

Conflict of Interest

The authors declare no conflict of interest.

Data Availability Statement

The data that support the findings of this study are available from the corresponding author upon reasonable request.

Keywords

aqueous zinc-ion batteries, Mo-doped, oxygen vacancies, synergistic effect, vanadium oxides

Received: June 24, 2024
Revised: August 12, 2024
Published online: September 5, 2024

---

[1] S. Chen, Y. Ying, L. Ma, D. Zhu, H. Huang, L. Song, C. Zhi, *Nat. Commun.* **2023**, *14*, 2925.
[2] J. Zheng, Q. Zhao, T. Tang, J. Yin, C. D. Quilty, G. D. Renderos, X. Liu, Y. Deng, L. Wang, D. C. Bock, C. Jaye, D. Zhang, E. S. Takeuchi, K. J. Takeuchi, A. C. Marschilok, L. A. Archer, *Science* **2019**, *366*, 645.
[3] X. Chen, J.-H. Liu, H. Jiang, C. Zhan, Y. Gao, J. Li, H. Zhang, X. Cao, S. Dou, Y. Xiao, *Energy Storage Mater.* **2024**, *65*, 103168.
[4] W. Deng, Z. Huang, Z. Zhou, C. Li, Y. Chen, Y. Zhou, C. Huang, J. Zhu, W. Zou, R. Zhu, Y. Xu, R. Li, *ACS Energy Lett.* **2023**, *8*, 3171.
[5] N. Shang, K. Wang, M. Wei, Y. Zuo, P. Zhang, H. Wang, Z. Chen, D. Zhong, P. Pei, *Adv. Funct. Mater.* **2023**, *33*, 2303719.
[6] S. Liu, H. Zhu, B. Zhang, G. Li, H. Zhu, Y. Ren, H. Geng, Y. Yang, Q. Liu, C. C. Li, *Adv. Mater.* **2020**, *32*, 2001113.
[7] Y. Bai, Y. Qin, J. Hao, H. Zhang, C. M. Li, *Adv. Funct. Mater.* **2024**, *34*, 2310393.
[8] T. Lv, G. Zhu, S. Dong, Q. Kong, Y. Peng, S. Jiang, G. Zhang, Z. Yang, S. Yang, X. Dong, H. Pang, Y. Zhang, *Angew. Chem., Int. Ed.* **2023**, *62*, 202216089.
[9] C. Zheng, Z.-H. Huang, F.-F. Sun, Y. Zhang, H. Li, Y. Liu, T. Ma, *Small* **2024**, *20*, 2306275.
[10] Y. Liu, C. Lu, Y. Yang, W. Chen, F. Ye, H. Dong, Y. Wu, R. Ma, L. Hu, *Adv. Mater.* **2024**, *36*, 2312982.
[11] F. Ye, R. Pang, C. Lu, Q. Liu, Y. Wu, R. Ma, L. Hu, *Angew. Chem., Int. Ed.* **2023**, *62*, 202303480.
[12] B. Sambandam, V. Mathew, S. Kim, S. Lee, S. Kim, J. Y. Hwang, H. J. Fan, J. Kim, *Chem* **2022**, *8*, 924.
[13] L. Ma, S. Chen, C. Long, X. Li, Y. Zhao, Z. Liu, Z. Huang, B. Dong, J. A. Zapien, C. Zhi, *Adv. Energy Mater.* **2019**, *9*, 1902446.
[14] B. Yong, D. Ma, Y. Wang, H. Mi, C. He, P. Zhang, *Adv. Energy Mater.* **2020**, *10*, 2002354.
[15] X. Ma, X. Cao, M. Yao, L. Shan, X. Shi, G. Fang, A. Pan, B. Lu, J. Zhou, S. Liang, *Adv. Mater.* **2022**, *34*, 2105452.
[16] D. Kundu, B. D. Adams, V. Duffort, S. H. Vajargah, L. F. Nazar, *Nat. Energy* **2016**, *1*, 16119.
[17] X. Wang, Z. Zhang, M. Huang, J. Feng, S. Xiong, B. Xi, *Nano Lett.* **2022**, *22*, 119.
[18] F. Liu, Z. Chen, G. Fang, Z. Wang, Y. Cai, B. Tang, J. Zhou, S. Liang, *Nano-Micro Lett.* **2019**, *11*, 25.
[19] S. Deng, Z. Yuan, Z. Tie, C. Wang, L. Song, Z. Niu, *Angew. Chem., Int. Ed.* **2020**, *59*, 22002.
[20] X. Wang, Y. Li, S. Wang, F. Zhou, P. Das, C. Sun, S. Zheng, Z.-S. Wu, *Adv. Energy Mater.* **2020**, *10*, 2000081.
[21] J. Zhang, R. Liu, C. Huang, C. Dong, L. Xu, L. Yuan, S. Lu, L. Wang, L. Zhang, L. Chen, *Nano Energy* **2024**, *122*, 109301.
[22] W. Wu, J. Liang, S. Ye, Z. Chen, W. Chen, X. Zhao, L. Zheng, Q. Zhang, J. Liu, *EcoEnergy* **2024**, *2*, 169.
[23] D. Li, Y. He, B. Chen, J. Xu, Q. Liu, S. Yang, W. Y. Lai, *EcoEnergy* **2024**, *2*, 311.
[24] J. Guo, B. He, W. Gong, S. Xu, P. Xue, C. Li, Y. Sun, C. Wang, L. Wei, Q. Zhang, Q. Li, *Adv. Mater.* **2024**, *36*, 2303906.
[25] J.-S. Park, J. H. Jo, Y. Aniskevich, A. Bakavets, G. Ragoisha, E. Streltsov, J. Kim, S.-T. Myung, *Chem. Mater.* **2018**, *30*, 6777.
[26] P. Liu, X. Zhang, J. Fei, Y. Shi, J. Zhu, D. Zhang, L. Zhao, L. Wang, J. Lai, *Adv. Mater.* **2024**, *36*, 2310591.
[27] Q. Zhang, S. Jiang, T. Lv, Y. Peng, H. Pang, *Adv. Mater.* **2023**, *35*, 2305532.
[28] Z. Peng, Y. Li, P. Ruan, Z. He, L. Dai, S. Liu, L. Wang, S. Chan Jun, B. Lu, J. Zhou, *Coordin. Chem. Rev.* **2023**, *488*, 215190.
[29] Y. Sun, H. Ji, Y. Sun, G. Zhang, H. Zhou, S. Cao, S. Liu, L. Zhang, W. Li, X. Zhu, H. Pang, *Angew. Chem., Int. Ed.* **2024**, *63*, 202316973.
[30] Q. Song, S. Zhou, S. Wang, S. Li, L. Xu, J. Qiu, *Chem. Eng. J.* **2023**, *461*, 142033.
[31] P. Luo, Z. Huang, G. Liu, C. Liu, P. Zhang, Y. Xiao, W. Tang, W. Zhang, H. Tang, S. Dong, *J. Alloy. Compd.* **2022**, *919*, 165804.
[32] Y. Liu, X. Xiao, X. Liu, L. L. Cui, Y. Gong, *J. Mater. Chem. A* **2022**, *10*, 912.
[33] F. Ming, H. Liang, Y. Lei, S. Kandambeth, M. Eddaoudi, H. N. Alshareef, *ACS Energy Lett.* **2018**, *3*, 2602.
[34] D. Jia, Z. Shen, Y. Lv, Z. Chen, H. Li, Y. Yu, J. Qiu, X. He, *Adv. Funct. Mater.* **2024**, *34*, 2308319.
[35] W. Yu, H. Huang, Y. Qin, D. Zhang, Y. Zhang, K. Liu, Y. Zhang, J. Lai, L. Wang, *Adv. Energy Mater.* **2022**, *12*, 2200110.
[36] Y. Wang, J. Song, W. Y. Wong, *Angew. Chem., Int. Ed.* **2023**, *62*, 202218343.
[37] Y. Song, L. Jing, R. Wang, J. Cui, M. Li, Y. Zhang, *J. Energy Chem.* **2024**, *89*, 599.
[38] Y. Zhang, Z. Li, M. Liu, J. Liu, *Chem. Eng. J.* **2023**, *463*, 142425.
[39] S. Tan, Y. Jiang, Q. Wei, Q. Huang, Y. Dai, F. Xiong, Q. Li, Q. An, X. Xu, Z. Zhu, X. Bai, L. Mai, *Adv. Mater.* **2018**, *30*, 1707122.
[40] L. Zhang, Y. Liu, Z. Zhao, P. Jiang, T. Zhang, M. Li, S. Pan, T. Tang, T. Wu, P. Liu, Y. Hou, H. Lu, *ACS Nano* **2020**, *14*, 8495.
[41] K. Zhu, S. Wei, H. Shou, F. Shen, S. Chen, P. Zhang, C. Wang, Y. Cao, X. Guo, M. Luo, H. Zhang, B. Ye, X. Wu, L. He, L. Song, *Nat. Commun.* **2021**, *12*, 6878.
[42] X. Wen, W. Feng, X. Li, J. Yang, R. Du, P. Wang, H. Li, L. Song, Y. Wang, M. Cheng, J. He, J. Shi, *Adv. Mater.* **2023**, *35*, 2211690.
[43] J. Zhao, D. Xiao, Q. Wan, X. Wei, G. Tao, Y. Liu, Y. Xiang, K. Davey, Z. Liu, Z. Guo, Y. Song, *Small* **2023**, *19*, 2301738.
[44] C. Li, X. Yun, Y. Chen, D. Lu, Z. Ma, S. Bai, G. Zhou, P. Xiao, C. Zheng, *Chem. Eng. J.* **2023**, *477*, 146901.
[45] Z. Chen, Z. Yu, L. Wang, Y. Huang, H. Huang, Y. Xia, S. Zeng, R. Xu, Y. Yang, S. He, H. Pan, X. Wu, X. Rui, H. Yang, Y. Yu, *ACS Nano* **2023**, *17*, 16478.

[46] Z. Pan, L. Jin, C. Yang, X. Ji, M. Liu, *Chem. Eng. J.* **2023**, *470*, 144084.

[47] Y. Liu, Y. Sun, J. Zhang, X. Hao, M. Zhang, P. Wei, X. Zhao, K. Cai, *Nano Energy* **2024**, *120*, 109152.

[48] K. Zhu, T. Wu, W. van den Bergh, M. Stefik, K. Huang, *ACS Nano* **2021**, *15*, 10678.

[49] J. Cao, D. Zhang, Y. Yue, X. Yang, C. Yang, J. Niu, Z. Zeng, P. Kidkhunthod, S. Wannapaiboon, X. Zhang, J. Qin, J. Lu, *Adv. Funct. Mater.* **2023**, *33*, 2307270.

[50] X. Gu, J. Wang, X. Zhao, X. Jin, Y. Jiang, P. Dai, N. Wang, Z. Bai, M. Zhang, M. Wu, *J. Energy Chem.* **2023**, *85*, 30.

[51] J. Guo, J. Liu, W. Ma, Z. Sang, L. Yin, X. Zhang, H. Chen, J. Liang, D. Yang, *Adv. Funct. Mater.* **2023**, *33*, 2302659.

[52] Q. Sun, H. Cheng, Y. Yuan, Y. Liu, W. Nie, K. Zhao, K. Wang, W. Yao, X. Lu, J. Lu, *Adv. Energy Mater.* **2023**, *13*, 2202515.

[53] D. Chen, Y. Liu, P. Feng, X. Tao, Z. Huang, X. Zhang, M. Zhou, J. Chen, *J. Energy Chem.* **2024**, *91*, 111.

[54] M. Wang, G. Zhao, X. Bai, W. Yu, C. Zhao, Z. Gao, P. Lyu, Z. Chen, N. Zhang, *Adv. Energy Mater.* **2023**, *13*, 2301730.

[55] H. Luo, B. Wang, F. Wang, J. Yang, F. Wu, Y. Ning, Y. Zhou, D. Wang, H. Liu, S. Dou, *ACS Nano* **2020**, *14*, 7328.

[56] L. Wang, K.-W. Huang, J. Chen, J. Zheng, *Sci. Adv.* **2019**, *5*, eaax4279.

[57] C. Xia, J. Guo, Y. Lei, H. Liang, C. Zhao, H. N. Alshareef, *Adv. Mater.* **2018**, *30*, 1705580.

[58] Y. Li, W. Yang, W. Yang, Y. Huang, G. Wang, C. Xu, F. Kang, L. Dong, *J. Energy Chem.* **2021**, *60*, 233.

[59] Y. Liu, J. Huang, X. Li, J. Li, J. Yang, K. Cai, *J. Energy Chem.* **2024**, *90*, 578.

[60] K. Zhu, T. Wu, K. Huang, *Energy Storage Mater.* **2021**, *38*, 473.

[61] X. Wang, Y. Wang, A. Naveed, G. Li, H. Zhang, Y. Zhou, A. Dou, M. Su, Y. Liu, R. Guo, C. C. Li, *Adv. Funct. Mater.* **2023**, *33*, 2306205.

[62] S. Zhao, S. Wang, J. Guo, L. Li, C. Li, Y. Sun, P. Xue, D. Wu, L. Wei, Y. Wang, Q. Zhang, *Adv. Funct. Mater.* **2023**, *33*, 2305700.